Current Chemistry Letters 15 (2026) 17–34

Contents lists available at GrowingScience

Current Chemistry Letters

homepage: www.GrowingScience.com

Mechanistic and stereoelectronic insights into the asymmetric diels–alder (4+2) cycloaddition toward cantharidin derivatives via DFT: Computational elucidation of their anticancer potential through docking, ADMET, and molecular dynamics analysis

Tarik Boutadghart[a*], Khadija Zaki[b], Youssef Merroun[a], Abdelouahid Sbai[b] and Rachida Ghailane[a]

[a]*Department of chemistry, Laboratory of Organic Chemistry, Catalysis and Environment, Ibn Tofail University, Faculty of Sciences, Po Box 133, 14000 Kenitra, Morocco*
[b]*Molecular Chemistry and Natural Substances Laboratory, Moulay Ismail University, Faculty of Science, Meknes, Morocco*

C H R O N I C L E

Article history:
Received April 15, 2025
Received in revised form
June 17, 2025
Accepted November 5, 2025
Available online
November 5, 2025

Keywords:
DFT
Norcantharimide
Blood Cancer
Molecular docking
ADMET
Molecular dynamics

A B S T R A C T

This investigation employs Molecular Electron Density Theory (MEDT) to elucidate the stereoselective (4+2) cycloaddition between 1-(furan-2-yl)propan-1-one and 1-R-1*H*-pyrrole-2,5-dione, combining mechanistic and pharmacological analyses. DFT calculations at the M06/6-311++G(d,p) level identified six distinct reaction pathways, revealing the exo cycloadduct as the thermodynamically favored product, consistent with experimental observations. Transition state analysis through NCI revealed stabilizing C*H*-π and van der Waals interactions governing the exo preference. Beyond mechanistic insights, the derived norcantharimide analogues exhibit promising anticancer potential, with strong binding affinities against hematological malignancy targets. SwissADME profiling confirmed optimal drug-likeness (QED > 0.6, TPSA < 100 Å²) and low hepatotoxicity risk. Notably, molecular dynamics simulations established exceptional stability for lead compound P2d (RMSD < 2.0 Å over 100 ns), with persistent hydrogen bonding (occupancy >75%) to key catalytic residues. These integrated computational results position these derivatives as viable candidates for blood cancer therapeutics, merging rigorous mechanistic understanding with preclinical potential assessment.

© 2026 by the authors; licensee Growing Science, Canada.

1. Introduction

The Diels-Alder reaction stands as a cornerstone of modern synthetic organic chemistry, offering unparalleled versatility in the construction of complex heterocyclic frameworks with significant biological and pharmacological relevance[1]. This (4+2) cycloaddition between a conjugated diene and a dienophile enables efficient access to structurally diverse compounds, with reaction efficiency governed by electronic and steric factors[2,3]. As established by Diels and Alder, optimal reactivity occurs when electron-rich dienes combine with electron-deficient dienophiles, a principle that has guided decades of synthetic applications[4]. The inherent complexity of asymmetric variants manifests in the formation of regio- and stereoisomeric adducts, where substituent orientation and steric constraints critically influence reaction outcomes[5]. Extensive mechanistic studies, employing both experimental[6,7] and theoretical[7-9] approaches, have elucidated the factors controlling selectivity patterns, particularly in the formation of seven-membered rings where dienophile regioselectivity and substituent bulk dominate the transition state geometry. Recent advances have further demonstrated how these fundamental principles can be harnessed to control molecular architecture in target-oriented synthesis, while contemporary mechanistic understanding continues to reveal new aspects of pericyclic control in complex systems[10,11]. The norcantharimide scaffold, particularly its ketone-substituted derivatives such as (4R,7S)-2-R-4-propionyl-3a,4,7,7a-tetrahydro-1H-4,7-epoxyisoindole-1,3(2H)-dione, represents a privileged structural motif in medicinal chemistry. These compounds are typically synthesized via Diels-Alder (4+2) cycloaddition between 1-(furan-2-yl)propan-1-one (diene) and 1-R-1H-pyrrole-2,5-dione (dienophile), as demonstrated by Cioc et al.[12]. By systematically examining both stationary points and electron density redistribution patterns, MEDT provides a comprehensive picture of reaction mechanisms that connects electronic structure changes with observed reactivity trends. This approach has proven particularly valuable for

* Corresponding author Tel.:
E-mail address Tarikboutadghart5@gmail.com (T. Boutadghart)
© 2026 by the authors; licensee Growing Science, Canada
doi: 10.5267/j.ccl.2025.11.004

understanding pericyclic reactions, where electron density reorganization dictates both reaction feasibility and selectivity patterns. The theory's emphasis on dynamic electron density analysis rather than static molecular properties offers a more nuanced understanding of organic reaction mechanisms and has become an essential tool in modern computational organic chemistry.

In this work, a thorough theoretical investigation was carried out to elucidate the reaction mechanism of the (4+2) cycloaddition between 1-(furan-2-yl)propan-1-one and 1-R-1H-pyrrole-2,5-dione (**Scheme 1**). Using Density Functional Theory (DFT), we systematically explored the factors governing the experimentally observed regioselectivity. Both global and local reactivity descriptors were employed to characterize the electrophilic and nucleophilic nature of the reactants, thereby offering valuable insights into their mutual interactions. Calculations of reaction energies and activation barriers were essential in rationalizing the preferential regioselective outcome. Moreover, the evolution of the bonding process along the intrinsic reaction coordinate (IRC) was analyzed using Electron Localization Function (ELF) and Non-Covalent Interaction (NCI) index topologies, allowing us to trace the formation of new sigma bonds and to visualize subtle electronic rearrangements during the course of the reaction. The primary goal of this study is to monitor variations in quantum chemical observables along the reaction path, assess the different possible addition modes, characterize the transition states involved, and ultimately identify the most favorable mechanistic route. It is noteworthy that several norcantharimide-based derivatives bearing aliphatic, azaaryl, or pyridyl substituents have shown potent cytotoxic and anticancer properties, particularly against HL-60 and Hep3B hepatocellular carcinoma cell lines[13-14]. Among the various norcantharimide derivatives, those incorporating a ketone functional group have attracted particular attention due to their distinctive capacity to stimulate leukocyte production within the bone marrow. In this context, the work of Lin et al. emphasized the therapeutic relevance of this structural class by successfully synthesizing several norcantharimide analogues, thereby contributing to the expansion of a promising library of anticancer compounds. In light of the notable anticancer activity previously reported for these molecules, it is crucial to assess the inhibitory potential of the ketone-functionalized norcantharimide derivatives designed and evaluated in the present theoretical study against hematological malignancies[15-16].

In this context, the second phase of our investigation aimed to evaluate the inhibitory potential of six ketone-substituted norcantharimide derivatives against hematological cancers. This was accomplished via molecular docking studies, which enabled the assessment of their binding affinities and interaction profiles with the Mpro protease, a key molecular target implicated in the progression of the disease. Furthermore, an ADMET (Absorption, Distribution, Metabolism, Excretion, and Toxicity) analysis was conducted to predict the pharmacokinetic behavior and safety profiles of these compounds in biological systems. To reinforce the reliability of the docking results, molecular dynamics (MD) simulations were performed, confirming the structural stability and persistence of the most promising ligand–protein complexes over time.

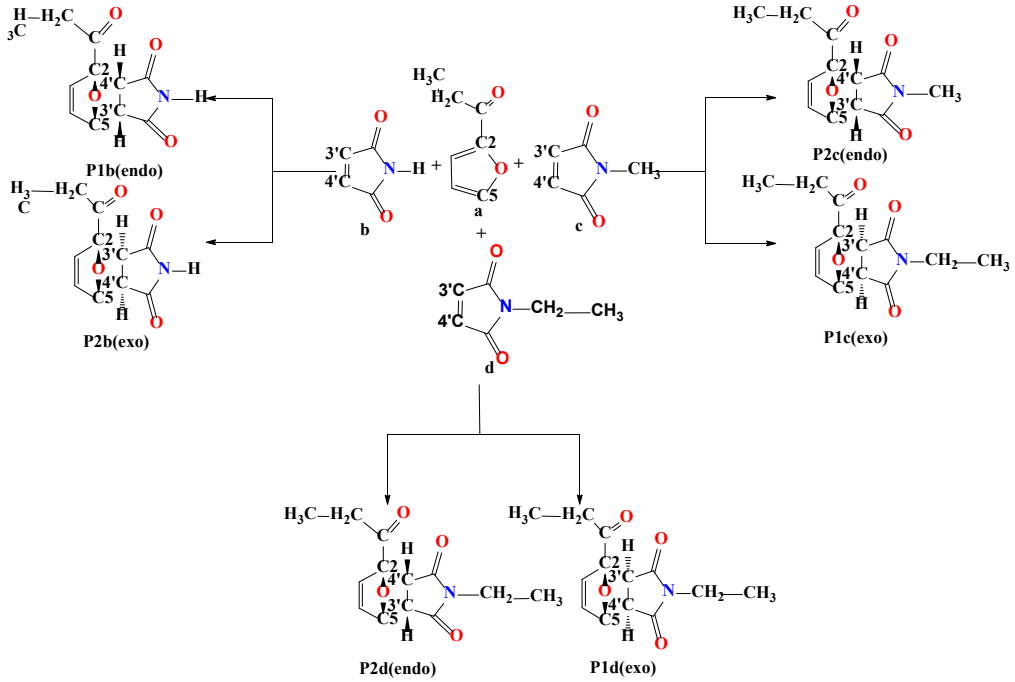

Scheme 1. The regio isomeric reaction pathways in the cycloaddition reaction of 1-(furan-2-yl)propan-1-one (**a**) with 1H-pyrrole-2,5-dione (**b**), 1-methyl-1H -pyrrole-2,5-dione (**c**) and 1-ethyl-1H-pyrrole-2,5-dione (**d**).

2. Theoretical background

2.1. MEDT Study

The stationary points along the reaction pathway of the (4+2) cycloaddition between 1-(furan-2-yl)propan-1-one and 1-R-1H-pyrrole-2,5-dione were optimized using Density Functional Theory (DFT) at the M06/6-311++G(d,p) level[17,18], as implemented in the Gaussian 16 software package[19] along with the graphical interface-GaussView-6.0. with GaussView 6.0 employed as the graphical user interface. Geometry optimizations for all species—including reactants, transition states, and products were performed using the Berny algorithm based on analytical gradients[20]. Vibrational frequency analyses at 298.15 K and 1 atm were carried out to characterize the nature of each stationary point: transition states (TS) were validated by the presence of a single imaginary frequency, while reactants and products displayed none. The intrinsic reaction coordinate (IRC) pathways were traced using the second-order Gonzalez–Schlegel algorithm[21] to confirm the connectivity of each transition state to its corresponding minima[22]. Solvent effects were incorporated by optimizing all gas-phase geometries within the polarizable continuum model (PCM), simulating water as the solvent (ε = 78.3553), as developed by Tomasi's group[23-25]. Furthermore, based on conceptual DFT, global reactivity descriptors—including the electronic chemical potential (μ), chemical hardness (η)[26], global electrophilicity index ω[26], and global nucleophilicity index N[27] were calculated to gain insight into the electronic nature of the reactants.

$$\mu = \frac{-(\mathrm{IP} + \mathrm{EA})}{2}, \qquad \mathrm{IP} = -\mathrm{E_{HOMO}}$$
$$\eta = (\mathrm{IP} - \mathrm{EA}), \qquad \mathrm{EA} = -\mathrm{ELUMO}$$
$$\omega = \frac{\mu^2}{2\eta}, \quad \mathrm{N} = \mathrm{E_{HOMO(nucleophile)}} - \mathrm{E_{HOMO(tetracyanoethylene)}}$$

In this study, the energies of the frontier molecular orbitals, namely EHOMO and ELUMO, were used to characterize the electronic properties of the reactants. The HOMO energy of tetracyanoethylene (EHOMO(TCNE)) was adopted as a reference, as this neutral molecule is widely recognized for its pronounced electrophilic behavior. The local electrophilic and nucleophilic Parr functions were obtained from the Mulliken atomic spin densities (ASD) of the corresponding radical cation and radical anion species, respectively. The global electron density transfer (GEDT) at the transition states (TSs) was evaluated using the expression GEDT $\sum$(f)= q$\in$f q, where q represents the natural bond orbital (NBO)-derived atomic charges[28]. To gain deeper insight into the electronic reorganization during the reaction, the electron localization function (ELF)[29] was analyzed using the Multiwfn software[30] based on mono-determinantal wavefunctions associated with selected structures. Additionally, the topological properties of the electron density were studied via Atoms-in-Molecules (AIM) theory[31] also implemented in Multiwfn, with the resulting isosurfaces visualized using Visual Molecular Dynamics (VMD 1.9.3)[32]. Furthermore, the nature and extent of non-covalent interactions were explored using the reduced density gradient (RDG) approach, commonly referred to as the Non-Covalent Interaction (NCI) method[33]. This technique is particularly useful for distinguishing the most favorable addition channels by identifying weak interactions within different transition structures. The RDG function is defined as $\mathrm{RDG}\ (\mathrm{r}) = \frac{1}{2(3\pi^2)^{\frac{1}{3}}} \frac{|\nabla\rho(r)|}{\rho(r)^{\frac{4}{3}}}$, where, $\rho(r)$ denotes the electron density, and $\nabla\rho(r)$ is the gradient of the electron density. Regions of low electron density and low RDG values typically correspond to non-covalent interactions such as van der Waals forces or hydrogen bonding[34].

2.2. In silico pharmacokinetics ADME/Tox and drug-likeness prediction

The ketone-substituted norcantharimide derivatives proposed in this study were further evaluated through comprehensive ADMET (Absorption, Distribution, Metabolism, Excretion, and Toxicity) profiling and drug-likeness prediction to assess their pharmacokinetic behavior and therapeutic potential. Key parameters such as gastrointestinal absorption, skin permeability, blood–brain barrier (BBB) penetration, cytochrome P450 (CYP) enzyme interactions, and various toxicity endpoints were analyzed. Additionally, synthetic accessibility and drug-likeness criteria were assessed according to Lipinski's Rule of Five, Veber's rule, and Ghose's filter. These evaluations were carried out using the SwissADME[35] and pkCSM[36] web-based platforms, which provide reliable in silico tools for early-stage drug discovery.

2.3. Docking protocol

The Protein Data Bank (PDB) constitutes a fundamental resource for accessing high-resolution crystallographic structures of proteins implicated in various cancers, including hematological malignancies. In this work, molecular docking simulations were performed to investigate the binding potential of the designed ketone-substituted norcantharimide derivatives against a key protease associated with blood cancer: the complement factor D, complexed with the inhibitor (S)-Pyrrolidine-1,2-dicarboxylic acid 1-[(1-methyl-1H-indol-3-yl)-amide] 2-[(3-trifluoromethoxy-phenyl)-amide], available under PDB ID: 5NAT[37]. The docking analysis provided insights into the predicted binding modes and affinities of the ligands, highlighting specific interactions with crucial amino acid residues within the enzyme's active site[38]. These results contribute to a deeper understanding of the molecular basis of inhibition and may guide the rational design and optimization of novel chemotherapeutic agents targeting blood cancer[39].

To complement and refine the molecular docking results, molecular dynamics (MD) simulations were conducted, providing a dynamic perspective on the stability and conformational behavior of the protein–ligand complexes over time. These simulations offered a comprehensive understanding of the flexibility of the active site and the persistence of key intermolecular interactions under physiological conditions. The crystallographic structure corresponding to PDB ID: 5NAT was obtained from the RCSB Protein Data Bank (https://www.rcsb.org/), and simulations were centered on the active site defined by the coordinates x: 1.318, y: –0.160, z: 13.222, using a docking grid dimension of 40 × 40 × 40 Å[40]. The resulting data provided valuable atomic-level insights into the binding mechanisms, thereby supporting the rational development of targeted inhibitors against blood cancer-associated proteases.

The preparation of protein and ligand structures in the .pdbqt format was carried out using AutoDock Tools version 1.5.6[41]. Ligands were initially sketched with GaussView 6.0, then geometrically optimized and saved in .pdb format prior to conversion into .pdbqt files. Molecular docking simulations were subsequently conducted using the most recent version of AutoDock Vina[42]. The resulting binding poses and interaction profiles were analyzed and visualized in both two-dimensional and three-dimensional representations using the Discovery Studio 2021 Client software[43].

2.4. Molecular dynamics simulation

Molecular dynamics (MD) simulations were conducted to assess the structural stability and conformational dynamics of the protein–ligand complex, utilizing the Desmond module integrated within the Schrödinger Suite 2018-4[44]. The system was prepared using the Protein Preparation Wizard, which allowed for the assignment of correct bond orders, addition of hydrogen atoms, and optimization of the hydrogen-bonding network. Ligand parameters were generated based on the OPLS4 force field. Solvation was performed using a TIP3P water model in an orthorhombic box with a 10 Å buffer distance, and appropriate counterions were added to neutralize the system. Energy minimization and equilibration steps were carried out using the default protocol provided by Desmond. The production phase consisted of a 100-nanosecond simulation under an NPT ensemble, maintaining a temperature of 300 K and a pressure of 1 atm via the Nose-Hoover thermostat and Martyna-Tobias-Klein barostat. Post-simulation analysis included key structural descriptors such as root-mean-square deviation (RMSD), root-mean-square fluctuation (RMSF), radius of gyration (Rg), and hydrogen bond occupancy, enabling a comprehensive evaluation of the dynamic stability and flexibility of the complex throughout the simulation timeframe.

3. Results and discussion

3.1. Analysis of the conceptual DFT indices of the separated reagents

Global indices analysis

To explore the local atomic characteristics of the reagents, reactivity indices derived from Conceptual Density Functional Theory (CDFT) were evaluated. The global descriptors—including electronic chemical potential (μ), chemical hardness (η), electrophilicity index (ω), and nucleophilicity index (N)—serve as valuable theoretical tools for rationalizing the behavior of species in cycloaddition reactions. The computed parameters for 1-(furan-2-yl)propan-1-one (a), 1H-pyrrole-2,5-dione (b), 1-methyl-1H-pyrrole-2,5-dione (c), and 1-ethyl-1H-pyrrole-2,5-dione (d) are summarized in **Table 1**. The electronic chemical potentials of the dienophiles b (–5.572 eV), c (–5.465 eV), and d (–5.440 eV) are lower than that of the diene a (–4.438 eV), indicating a favorable charge transfer from the diene to the dienophiles under normal electron demand (NED) conditions. This trend is further supported by the chemical hardness values, which show that diene a (η = 5.662 eV) is slightly less reactive compared to dienophiles b (η = 5.392 eV), c (η = 5.403 eV), and d (η = 5.411 eV).

The nucleophilicity index (N) of diene a (2.099) is notably higher than those of dienophiles b, c, and d (1.099, 1.202, and 1.222, respectively). According to Domingo's classification, nucleophiles are categorized as strong when N > 3 eV, moderate when 2 eV < N < 3 eV, and marginal when N < 2 eV[45]. Based on this scale, diene a is considered a moderate nucleophile. In contrast, the electrophilicity index (ω) values for dienophiles b (2.879), c (2.763), and d (2.734) exceed that of diene a (1.739), indicating a higher tendency of the dienophiles to act as electrophiles. According to the absolute electrophilicity scale proposed by Domingo, molecules with ω > 2.2 are classified as strong electrophiles[46]. These findings confirm the electronic nature of the reactants, with diene a functioning as a nucleophile and dienophiles b, c, and d behaving as strong electrophiles.

Table 1. The electronic chemical potential μ, chemical hardness η, electrophilicity ω and nucleophilicity N of 1-(furan-2-yl)propan-1-one (**a**), 1H-pyrrole-2,5-dione (**b**), 1-methyl-1H-pyrrole-2,5-dione (**c**) and 1-ethyl-1H-pyrrole-2,5-dione (**d**).

	μ	η	ω	N
Diene a	-4.43	5.66	1.73	2.09
Dienophile b	-5.57	5.39	2.87	1.09
Dienophile c	-5.46	5.40	2.76	1.20
Dienophile d	-5.44	5.41	2.73	1.22

Local indices analysis

In 2013, Domingo et al.[47], introduced the concept of local reactivity descriptors to characterize the electrophilic and nucleophilic sites within a molecule. They defined the electrophilic local reactivity index as $P^{+k}=\rho_s^{ra}(r)$ and the nucleophilic local reactivity index as $P^{-k}=\rho_s^{rc}(r)$, where these indices are derived from Parr functions. These functions are calculated based on the Mulliken atomic spin densities (MASD) of the radical anion and radical cation at the corresponding atomic sites, using single-point energy calculations performed at the geometry of the neutral species. **Fig. 1** presents the three-dimensional Parr function maps of the studied reagents. Analysis of the nucleophilic Parr function for diene a reveal that the C5 atom C5 = 0.43, exhibits a slightly higher nucleophilic character than C2 = 0.42. Regarding dienophile **b**, the electrophilic Parr function shows equal reactivity at the C3′ and C4′ positions (P^{+k} = 0.24), which can be attributed to the molecular symmetry of the dienophile. Consequently, two possible cycloaddition pathways may occur: one involving interactions between C5 with C3' and C2 with C4' and the other between C5 and C4' and C2 with C3'. These pathways correspond to the formation of two regioisomeric products, designated as P1b (exo) and P2b (endo). For dienophile **c**, the analysis of the electrophilic Parr functions reveals that the C3'and C4' carbon atoms possess identical values (0.24), a result of the molecular symmetry of the compound. This symmetry suggests two possible modes of nucleophilic attack: either C5 of the diene a interacts with C3′ and C2 with C4′, or C5 interacts with C4′ and C2 with C3′. These two orientations are consistent with the formation of the regioisomeric products P1c (exo) and P2c (endo). Similarly, in the case of dienophile d, the electrophilic Parr function yields equal values for C3′ and C4′ (0.24), again indicating symmetrical reactivity. As with the previous case, this allows for two potential interaction pathways: the C5 atom of the diene may preferentially attack C3′ of the dienophile, while C2 targets C4′, or the inverse may occur, with C5 attacking C4′ and C2 attacking C3′. These interaction modes lead to the possible formation of the regioselective products P1d (exo) and P2d (endo).

Table 2. Global electron density transfer (GEDT, in e) of all transition states.

	TS1b(exo)	TS2b(endo)	TS1c(exo)	TS2c(endo)	TS1d(exo)	TS2d(endo)
GEDT(e)	0.27	0.20	0.35	0.17	0.32	0.16

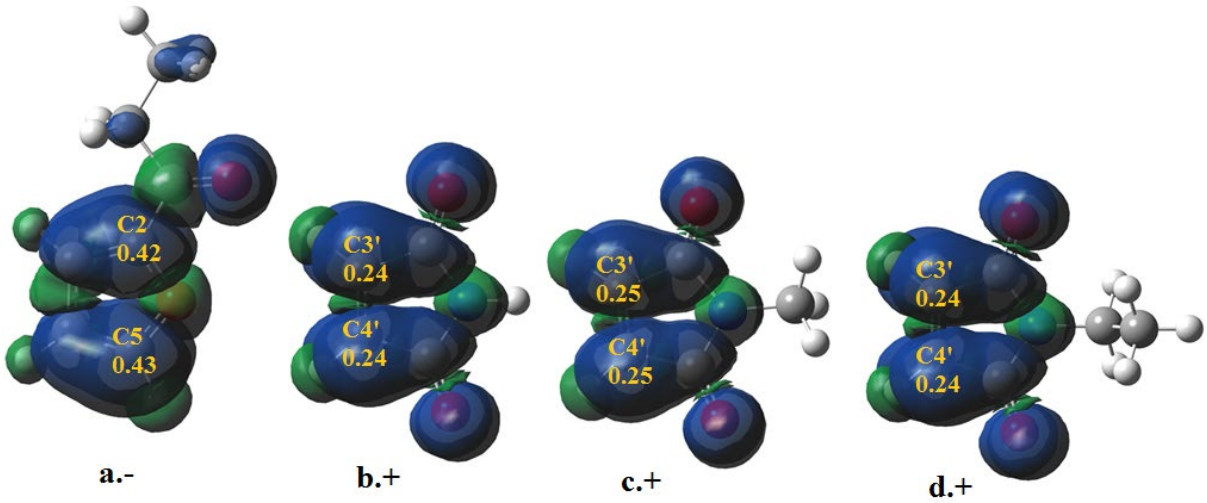

Fig. 1. The functions of Parr of the reagents.

To assess the charge transfer (CT) occurring during the (4+2) cycloaddition reactions, the global electron density transfer (GEDT) was calculated at the transition states (TSs). This was achieved through Natural Bond Orbital (NBO) analysis, by evaluating the distribution of natural atomic charges between the nucleophilic and electrophilic fragments[48] A positive GEDT value indicates electron flow from the diene to the dienophile. The computed results, summarized in **Table 2**, demonstrate that in all cases, the charge transfer occurs from the diene to the dienophile, corroborating the findings from the conceptual DFT (CDFT) indices and confirming the normal electron demand (NED) character of the reactions. Moreover, the GEDT values range from 0.16 to 0.35e, which are all greater than 0.1e, suggesting that the investigated Diels–Alder reactions exhibit a significant polar character[49].

3.2. Energetic study

Due to the asymmetric nature of the reactants, the cycloaddition is expected to proceed through two competing regioselective pathways: exo and endo. The (4+2) cycloaddition between 1-(furan-2-yl)propan-1-one and 1-R-1H-pyrrole-2,5-dione follows a concerted, one-step mechanism. The transition states corresponding to each pathway have been identified and labeled as TS1b (exo), TS2b (endo), TS1c (exo), TS2c (endo), TS1d (exo), and TS2d (endo). The resulting cycloadducts—P1b (exo), P2b (endo), P1c (exo), P2c (endo), P1d (exo), and P2d (endo) were fully optimized and

characterized using computational methods. The relative energy profiles, enthalpy energy and Gibs free energy are shown in **Fig. 2(a-c)**, and additional thermodynamic and kinetic data are provided in **Table S1**. The calculated activation energies indicate that the energy barriers for TS1b (exo, 14.5 kcal/mol) and TS2b (endo, 14.6 kcal/mol) are nearly identical, implying that both reaction channels are kinetically accessible. Furthermore, the formation of the corresponding products P1b and P2b is exothermic, highlighting their thermodynamic stability.

From a thermodynamic standpoint, the exo regioisomer P1b is predicted to be more stable than its endo analogue P2b by 5.1 kcal/mol, aligning well with experimental findings. In the second reaction, the computed activation energy for the exo transition state TS1c (13.9 kcal/mol) is slightly lower than that for the endo transition state TS2c (14.3 kcal/mol), with a difference of 0.4 kcal/mol. This small but significant disparity indicates a kinetically favored exo pathway, reinforcing the observed regioselectivity. Additionally, the process is exothermic, with enthalpy changes of −16.1 kcal/mol and −11.8 kcal/mol for the formation of P1c (exo) and P2c (endo), respectively, further confirming the thermodynamic preference for the exo product. In the third system, the energy barrier difference between the exo and endo routes is estimated at 0.5 kcal/mol, again suggesting a slight kinetic advantage for the exo pathway. From a thermodynamic perspective, P1d (exo) is favored over P2d (endo) by 4.2 kcal/mol. These computational insights are consistent with experimental product ratios, which report 61% yield for P1d (exo) and only 4% for P2d (endo), thereby substantiating the regioselective nature of the cycloaddition process

The impact of solvation on the reaction mechanism was assessed by performing full geometry optimizations of all stationary points in aqueous medium at 348 K, using the M06 functional with the 6-311++G(d,p) basis set. Solvent effects were incorporated through the Self-Consistent Reaction Field (SCRF) approach, employing the Polarizable Continuum Model (PCM) as formulated by Tomasi[50]. The computed energy data are reported in **Table S1**. The presence of water as a solvent significantly influenced both the kinetic and thermodynamic parameters of the reactions. For the first reaction, the activation energies showed slight increases of 0.2 kcal/mol for TS1b (exo) and 0.8 kcal/mol for TS2b (endo), while the thermodynamic stabilities of the corresponding products declined by 2.4 kcal/mol (P1b, exo) and 1.3 kcal/mol (P2b, endo). These variations indicate a notable solvent effect in modulating reactivity. In the case of the second reaction, water induced minor increases in activation energies 0.6 kcal/mol for TS1c (exo) and 0.7 kcal/mol for TS2c (endo) accompanied by decreased product stability of 2.4 kcal/mol and 2.1 kcal/mol for P1c (exo) and P2c (endo), respectively. Similarly, for the third reaction, the activation energy barriers rose by 0.4 kcal/mol for TS1d (exo) and 0.7 kcal/mol for TS2d (endo), with corresponding reductions in product stability of 3.5 kcal/mol (P1d, exo) and 1.5 kcal/mol (P2d, endo). Overall, these findings suggest that solvation in water results in a moderate increase in activation barriers and a reduction in product stability. However, the observed regioselectivity of the reactions remains essentially unchanged, demonstrating the robustness of the regioselective outcome under solvated conditions.

Analysis of the enthalpy changes (ΔH) presented in **Table S1 and Fig. 2-b** shows that, in both media, all three exo pathways are thermodynamically more favored than their corresponding endo counterparts. This trend mirrors the behavior obtained for ΔE and reinforces the consistency between our theoretical predictions and the regioselectivity observed experimentally. According to the **Fig. 3-c**, the examination of the Gibbs free energy profiles further reveals that, for the first reaction, the activation free energy associated with the endo pathway (32.3 kcal/mol) is slightly lower than that of the exo pathway, indicating that, in this case, the endo approach is kinetically preferred despite being thermodynamically less favorable. Conversely, for the second and third reactions, the exo transition states display lower activation free energies than the corresponding endo transition states in both phases, supporting a kinetically favored exo addition for these systems. Overall, incorporation of solvent effects leads to a modest decrease in the activation barriers across the three reactions, without altering the predicted regioselectivity of the cycloaddition processes.

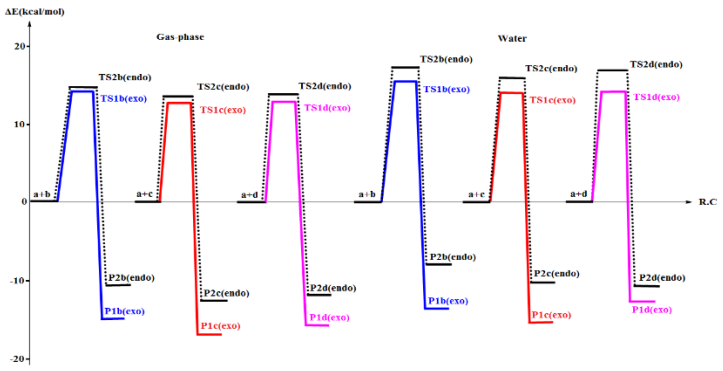

Fig. 2-a. Energy in kcal/mol, for the examined reaction paths associated with the [4+2] cycloaddition of 1-(furan-2-yl)propan-1-one (a), with 1H-pyrrole-2,5-dione (b), 1-methyl-1H-pyrrole-2,5-dione (c), and 1-ethyl-1H-pyrrole-2,5-dione (d) in the gas phase and in solution at M06/6–311++G(d,p).

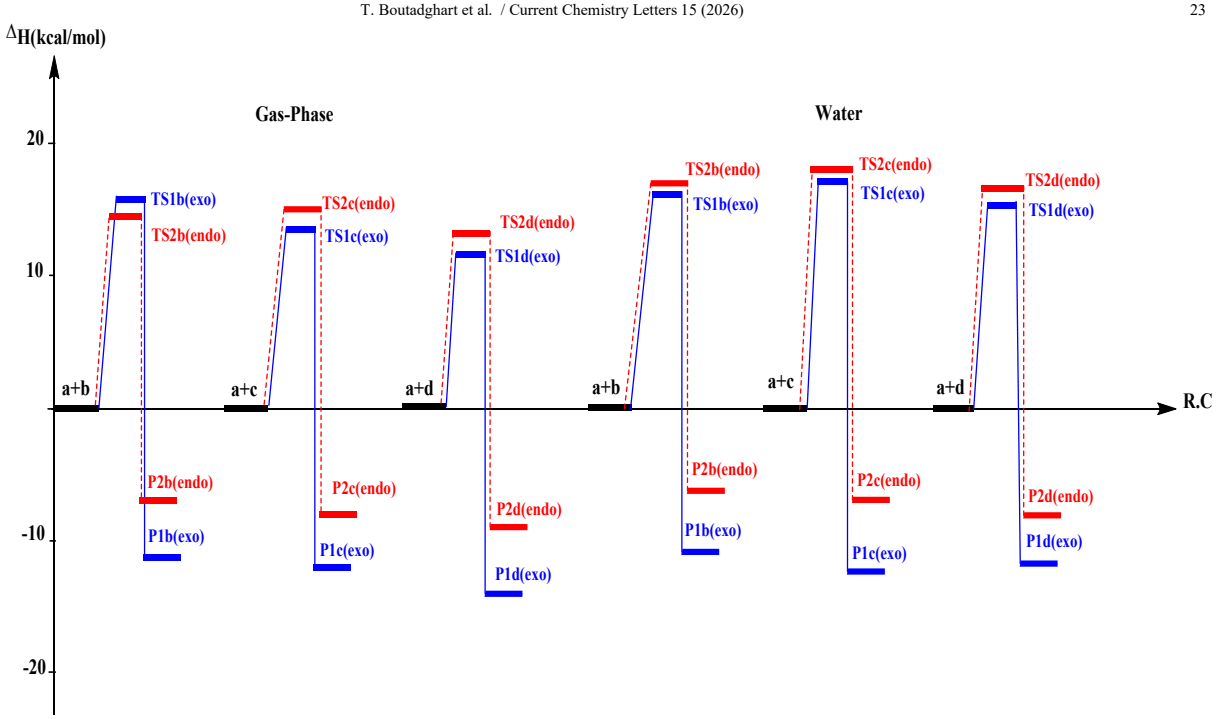

Fig. 2-b. Relative enthalpy energy in kcal/mol, for the reaction pathways examined associated with the [4+2] cycloaddition of 1-(furan-2-yl)propan-1-one (a), with 1H-pyrrole-2,5-dione (b), 1-methyl-1H-pyrrole-2,5-dione (c) and 1-ethyl-1H-pyrrole-2,5-dione (d) in gas phase and in solution at M06/6–311++G(d,p).

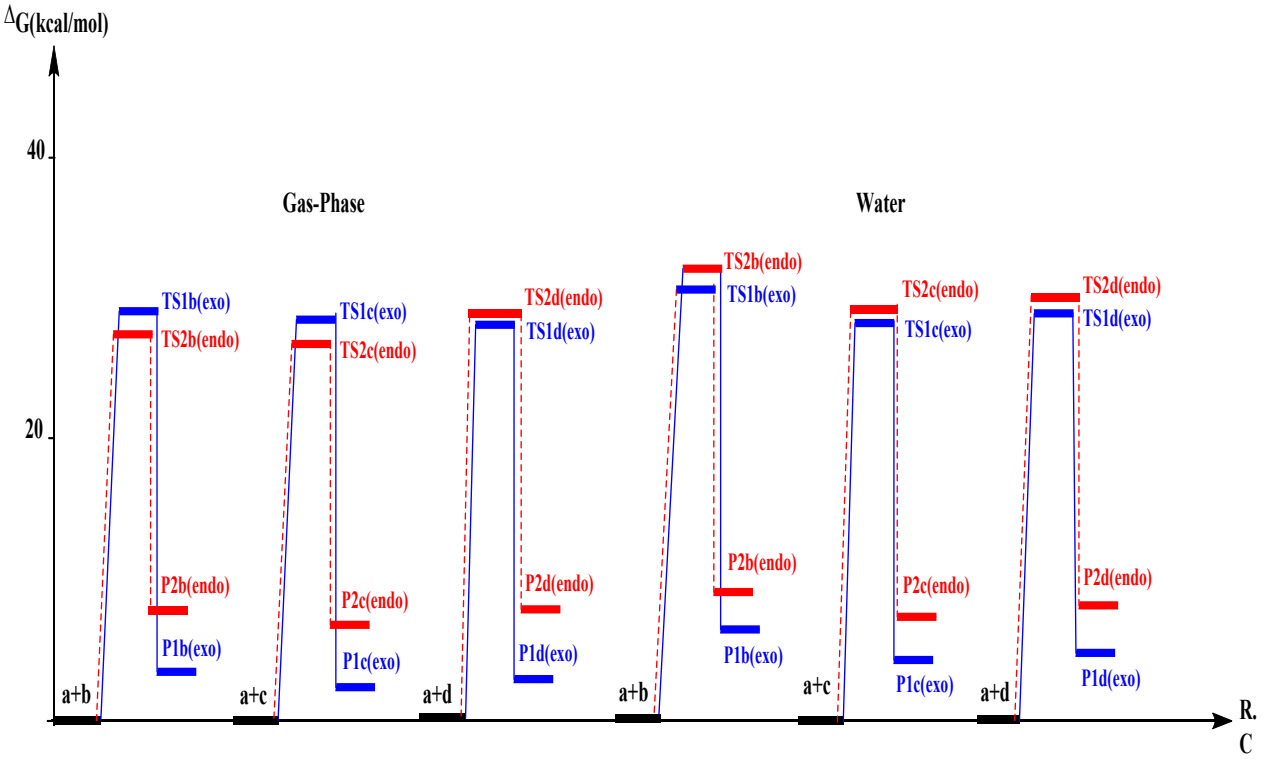

Fig. 2-c. Relative Gibbs free energy in kcal/mol, for the reaction pathways examined associated with the [4+2] cycloaddition of 1-(furan-2-yl)propan-1-one (a), with 1H-pyrrole-2,5-dione (b), 1-methyl-1H-pyrrole-2,5-dione (c) and 1-ethyl-1H-pyrrole-2,5-dione (d) in gas phase and in solution at M06/6–311++G(d,p).

Table 3. Key energy transition state parameters of the [4+2] cycloaddition of 1-(furan-2-yl)propan-1-one (a) with 1H-pyrrole-2,5-dione (b), 1-methyl-1H-pyrrole-2,5-dione (c) and 1-ethyl-1H-pyrrole-2,5-dione (d), in gas phase and in solution, calculated at level M06/6-311++G(d,p).

Stationary points	Gas phase					Water				
	E(u.a)	**ΔE**	**ΔH**	**ΔG**	**ΔS**	E(u.a)	**ΔE**	**ΔH**	**ΔG**	**ΔS**
TS1b(exo)	-781.1	14.5	15.1	29.9	-49.7	-781.1	14.7	15.4	33.1	-50.8
TS2b(endo)	-781.1	14.6	14.8	28.8	-54.8	-781.1	15.5	15.9	32.3	-47.1
TS1c(exo)	-820,4	13.7	14.9	29.2	-48.2	-820.4	14.3	15.7	31.8	-46.1
TS2c(endo)	-820.4	14.3	15.1	27.7	-42.4	-820.4	15.1	16.3	31.9	-44.5
TS1d(exo)	-859.6	14.0	14.3	29.6	-51.6	-859.7	14.4	15.1	32.5	-50.1
TS2d(endo)	-859.6	14.4	14.9	29.8	-50.2	-859.7	15.2	15.7	32.6	-48.5

3.3. Geometries of transition structures analysis

The optimized geometries and key interatomic distances of the transition states (TSs) involved in the cycloaddition reaction between 1-(furan-2-yl)propan-1-one (a) and maleimide derivatives (b–d) are illustrated in **Figs. 3 and S1**.

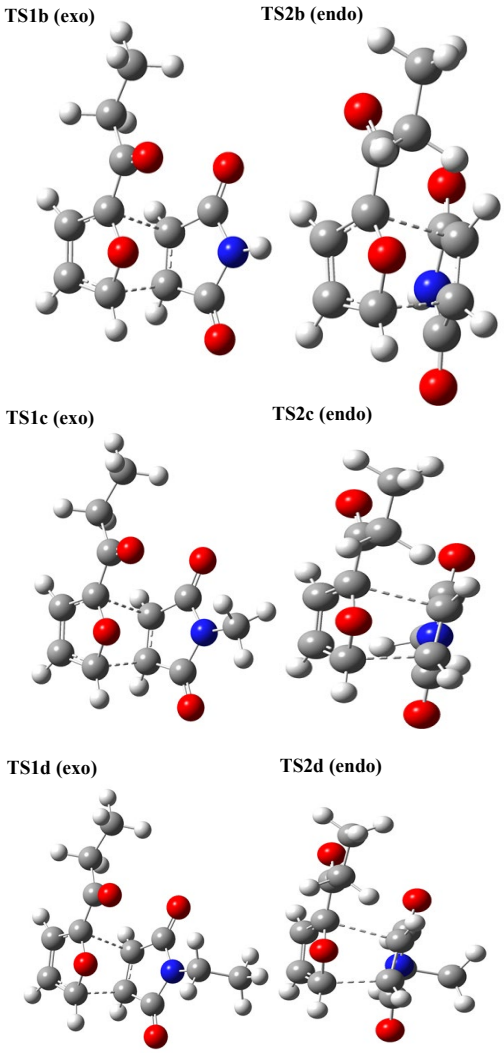

Fig. 3. Optimized geometries of the transition structures implying in the reaction pathways of the studied DA cycloadditions.

For the exo-transition pathways, the calculated bond-forming distances C5–C4′ and C2–C3′ are 1.982 Å and 2.335 Å for TS1b (exo), 1.974 Å and 2.355 Å for TS1c (exo), and 1.977 Å and 2.354 Å for TS1d (exo), respectively. In contrast, the

corresponding distances for the endo-transition pathways, C5–C3′ and C2–C4′, are determined to be 2.006 Å and 2.274 Å for TS2b (endo), 2.002 Å and 2.291 Å for TS2c (endo), and 2.016 Å and 2.273 Å for TS2d (endo), respectively. These geometric parameters reveal a pronounced degree of asynchronicity in the transition states, evidenced by the non-equivalent progression of bond formation at the reactive centers. This asynchronous character is likely governed by a combination of electronic and steric effects, which collectively influence the regioselectivity and kinetic accessibility of the cycloaddition pathway, thereby offering mechanistic insights into the reaction course. The degree of asynchronicity (Δd, in Å) is quantified as the difference between the lengths of the two forming σ-bonds in each transition state, corresponding to distinct positional modes of cycloaddition. The relatively small Δd values observed for the exo transition states (ranging from 0.335 to 0.381 Å) and for the endo transition states (ranging from 0.257 to 0.268 Å) provide compelling evidence for a concerted yet asynchronous one-step reaction mechanism. These findings underscore the unequal development of bond formation at the reactive centers, which is consistent with typical features of pericyclic reactions influenced by electronic and steric asymmetries.

3.3. ELF topologic analysis

ELF topologic analysis of the two C-C bonds formation along the DA reactional pathway of 1-(furan-2-yl)-propan-1-one (a) and 1-methyl-1H-pyrrole-2,5-dione (c)

This study aimed to elucidate the electronic features governing the most favorable pathway of the (4+2) cycloaddition reaction between 1-(furan-2-yl)propan-1-one (a) and 1-methyl-1H-pyrrole-2,5-dione (c). To characterize the redistribution of electron density throughout the reaction, a topological analysis of the Electron Localization Function (ELF)[51] was carried out along the Intrinsic Reaction Coordinate (IRC) associated with the lowest-energy transition state, TS1c (exo). This approach allowed for a fine-grained depiction of the electronic reorganization accompanying the bond formation process. The ELF analysis clearly reveals the separation of the diene (a) and the dienophile (c), and the locations of ELF attractors related to the emergence of the C5–C4′ and C2–C3′ σ-bonds are shown in **Fig. 4**.

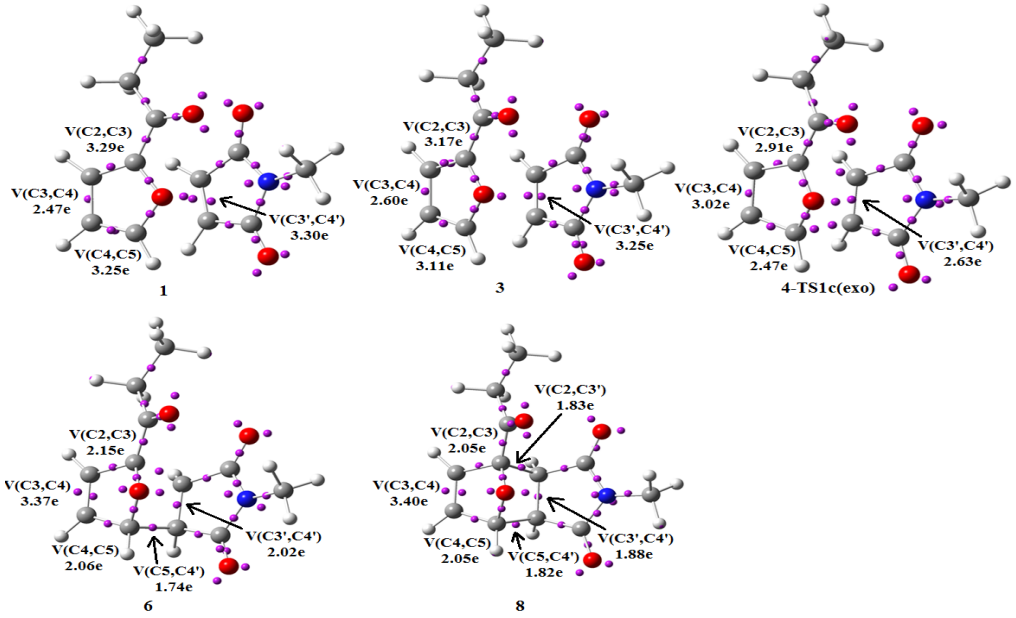

Fig. 4. ELF attractor's positions of the structure involved in the formation of single bonds. (the red color the oxygen atom, gray carbon atom, blue nitrogen atom, white hydrogen atom).

Furthermore, the evolution of the electronic populations of the most significant ELF valence basins along the IRC is detailed in **Table S3**. The results indicate that the formation of the C5–C4′ and C2–C3′ bonds follow a two-stage, concerted mechanism, providing further evidence for an asynchronous, one-step cycloaddition process. A comprehensive analysis of the ELF valence basins along the series of structures S1 to S8 reveals key electronic and structural features that characterize the progression of the cycloaddition reaction. At the initial stage (S1), two significant disynaptic basins, V(C2–C3) and V(C4–C5), exhibit electron populations of 3.29e and 3.27e, respectively, associated with bond lengths of 1.34 Å and 1.31 Å. These values suggest a pseudo-double bond character for both the C2=C3 and C4=C5 interactions. Additionally, the disynaptic basins V(C3′–C4′) and V(C3–C4) display electron populations of 3.27e and 2.47e, corresponding to bond distances of 1.32 Å and 1.40 Å, respectively. This electronic distribution is consistent with a double bond nature for C3′=C4′ and a single bond for C3–C4. The ELF topology at the S1 stage closely mirrors that of the isolated reactants, namely the diene (a) and the dienophile (b), highlighting minimal perturbation in electronic structure prior to bond formation. As the reaction proceeds, critical changes are observed at the S4 stage, where the emergence of three monosynaptic basins localized

at C2, C3′, and C4′—with electron populations of 1.02e, 0.41e, and 0.23e, respectively—marks the onset of new σ-bond formation.

Further along the reaction coordinate, at the S6 stage, the C5–C4′ bond is fully established, characterized by a bond length of 1.82 Å and an electron population of 1.74e within the corresponding disynaptic basin. This bond formation is facilitated by electron density transfer from the C3 carbon atom toward the developing pseudoradical center at C4 of the furan moiety, indicating a localized reorganization of electron density that drives the cycloaddition process. The disappearance of the monosynaptic basins V(C2) and V(C5) during the S6, S7, and S8 stages can be attributed to their involvement in reinforcing the stability of the C3–C4 double bond region. As the reaction advances, the formation of the second σ-bond, C2–C3′, occurs with a bond length of 1.54 Å and is characterized by a substantial electron population of 1.83e. This bond results from the coupling of pseudoradical centers localized in the monosynaptic basins V(C3) and V(C4) observed at the S8 stage. Subsequently, the system undergoes structural relaxation, leading to the formation of the thermodynamically most stable cycloadduct, P1c (exo).

3.4. Non-covalent interaction analysis (NCI)

The Non-Covalent Interaction (NCI) approach offers a powerful and insightful framework for the qualitative analysis of weak intermolecular and intramolecular interactions. Originally introduced by Yang et al.[52], through quantum mechanical calculations of the electron density, the NCI index serves as an effective visualization tool to distinguish between stabilizing and destabilizing non-covalent forces. This method proves particularly advantageous in highlighting subtle interactions such as van der Waals forces and steric effects—that are often inadequately captured by traditional analytical techniques. The spatial distribution of these interactions is rendered through a color-coded isosurface representation (**Fig. S3**), where strong attractive interactions appear in blue, strongly repulsive regions in red, and weak van der Waals interactions in green[53]. Notably, the green regions may reflect either favorable or unfavorable dispersion forces, depending on the molecular context. To deepen the understanding of these interactions along the reaction coordinates, the Reduced Density Gradient (RDG) isosurfaces and corresponding two-dimensional NCI scatter plots[54] were analyzed for all transition states (TS) involved in three (4+2) cycloaddition mechanisms, comprising a common diene (a) and three different dienophiles (b–d). The resulting three-dimensional RDG visualizations and associated scatter plots are depicted in **Fig. S4** and **Fig. S5**, respectively.

The Reduced Density Gradient (RDG) scatter plots, coupled with the second eigenvalue (λ_2) of the electron density Hessian matrix, were generated using the Multiwfn 3.6 program[30]. The underlying wavefunctions were computed at the M06/6-311++G(d,p) level of theory, and graphical representations were subsequently produced using the Gnuplot software[55]. Within the framework of Non-Covalent Interaction (NCI) analysis, the RDG and the quantity sign(λ_2)ρ the product of the sign of λ_2 and the electron density (ρ) serve as essential descriptors for detecting and characterizing weak interactions. **Fig S4** presents the RDG vs. sign(λ_2)ρ scatter plots corresponding to the six transition states (TSs) evaluated in this study. These visualizations enable a detailed interpretation of the dominant non-covalent interactions within each transition state. Specifically, three interaction domains can be distinguished: a blue region (−0.05 to −0.02 a.u.), indicative of strong attractive forces such as hydrogen bonding; a green region (−0.02 to 0.0080 a.u.), associated with weak van der Waals interactions and a red region (0.0080 to 0.05 a.u.), corresponding to steric repulsion. Comparative analysis of the TSs in both exo and endo orientations highlights variations in the intensity and spatial distribution of these interactions, offering insights into the stereochemical preferences of the cycloaddition processes. A thorough examination of the point cloud distributions corresponding to the analyzed transition states (TSs) reveals a subtle expansion of the red region, indicative of increased steric repulsion, accompanied by a slight contraction of the green region associated with weak van der Waals interactions. Additionally, the blue region typically associated with attractive interactions shows a modest increase in spatial extent. The analysis of δg_{inter} isosurfaces for all TSs, illustrated in **Fig. S5**, uncovers the presence of pronounced covalent interactions at the C5–C4′ and C2–C3′ bonding regions, as evidenced by the intense blue isosurfaces. In particular, the perforated nature of the blue isosurface around the C5–C4′ bond suggests a more advanced covalent character in this region relative to the C2–C3′ bond. This spatial differentiation supports the mechanistic hypothesis that the formation of the C5–C4′ bond precedes that of the C2–C3′ bond, aligning with a concerted yet asynchronous two-stage, one-step cycloaddition mechanism. Moreover, the appearance of red isosurfaces in the NCI analysis of the TSs points to significant steric hindrance effects, which are attributed to the presence of bulky substituents such as COEt, CH_3, and CH_2CH_3 on the reacting species.

3.5. Pharmacokinetic properties and ADMET results of the proposed new norcantharimide derivative

Drug-likeness refers to a multifaceted set of molecular and physicochemical attributes that influence a compound's potential to become a viable therapeutic agent[56]. Among the most widely adopted criteria for evaluating drug-likeness is Lipinski's Rule of Five, which postulates that compounds are more likely to exhibit favorable oral bioavailability and membrane permeability if they possess a molecular weight below 500 Da, a logP value less than 5, no more than 10 hydrogen bond acceptors, and fewer than 5 hydrogen bond donors. In the present study, the drug-likeness profiles of six novel norcantharimide-based compounds (**Figs. S6**) were assessed using the SwissADME and pkCSM web platforms. The computed descriptors are summarized in **Table 4**. The obtained results indicate that the designed molecules exhibit

physicochemical properties compatible with efficient oral absorption and permeability. Furthermore, a total polar surface area (TPSA) below 140 Å² and a limited number of rotatable bonds (nrotb < 10) are generally considered favorable for enhanced bioavailability and molecular flexibility, which are critical for optimal binding interactions with biological targets[57]. The three newly proposed derivatives, in particular, fulfill these criteria, supporting their potential as orally active drug candidates (**Table 4**). In addition, the synthetic accessibility (SA) of these norcantharimide derivatives, especially those bearing ketone functionalities, was evaluated to determine their feasibility for laboratory synthesis. As shown in **Table 4**, all candidates exhibit SA scores near 5 and below the threshold of 10, indicating acceptable synthetic tractability[58]. Lastly, a comprehensive ADMET analysis encompassing absorption, distribution, metabolism, excretion, and toxicity was conducted using SwissADME tools, with the full dataset presented in **Tables S4**, **S5**, and **S6**.

Table 4. Prediction of molecular properties parameters of the newly designed inhibitors and Enasidenib.

	Property									
	Formule	MW	HBD	HBA	nRot	Log P	TPSA	Log S	SA	Csp3
P1b/P2b(exo/endo)	$C_{11}H_{11}NO_4$	221.21	1	4	2	0	72.47	-1.28	3.80	0.55
P1c/ P2c(exo/endo)	$C_{12}H_{13}NO_4$	235.24	2	4	0	0.27	63.68	-0.91	3.90	0.58
P1d/P2d(exo/endo)	$C_{13}H_{15}NO_4$	249.26	0	4	3	0.63	63.68	-1.31	4.00	0.62
Enasdenib	$C_{19}H_{17}F_6N_7O$	437.37	3	12	8	3.62	108.74	-4.86	3.18	0.32

Absorption and Distribution

Transdermal drug delivery systems offer a promising alternative for both localized and systemic therapeutic applications. Nevertheless, the skin's stratum corneum, while serving as a critical barrier against environmental and chemical insults, poses a major challenge to the effective transdermal transport of pharmacologically active compounds. In this context, the assessment of human intestinal absorption (HIA) revealed encouraging results for the newly synthesized molecules, with predicted absorption rates ranging from 77.973% to 92.498%, reflecting favorable oral bioavailability. Additionally, the capacity of the compounds to permeate the blood–brain barrier (BBB) a highly selective physiological interface that restricts the passive diffusion of xenobiotics into the central nervous system was evaluated using the logBB parameter. Typically, compounds exhibiting logBB values below 0 are considered poorly brain-penetrant. As presented in **Tables S5** and **S6**, the designed molecules displayed efficient BBB permeability, in contrast to Enasidenib, which showed the lowest predicted brain distribution among the tested compounds. Despite these favorable pharmacokinetic properties, the investigated derivatives exhibit limited transdermal permeability, as reflected by their negative log Kp values, highlighting the persistent barrier function of the skin to these molecular structures.

Metabolism

The evaluation of cytochrome P450 (CYP) enzyme inhibition plays a critical role in anticipating potential drug–drug interactions and delineating toxicity risks during drug development. The biotransformation of the majority of xenobiotics and therapeutic agents is predominantly mediated by five key CYP isoforms: CYP1A2, CYP2C9, CYP2C19, CYP2D6, and CYP3A4. These enzymes are central to hepatic metabolism and significantly influence the pharmacokinetic profiles of drugs.

In the current study, the derivatives P1b/P2b (exo/endo), P1c/P2c (exo/endo), and P1d/P2d (exo/endo) emerged as strong inhibitors, exhibiting marked inhibitory potential across all five major CYP isoforms. Notably, these compounds are not predicted to act as substrates for either CYP2D6 or CYP3A4 (**Table S6**), which suggests a lower risk of rapid metabolic clearance via these pathways. Consequently, their pronounced inhibitory effects may significantly modulate their own metabolic fate and enhance systemic bioavailability, while also raising the potential for interaction with co-administered drugs metabolized by the same enzymes.

Excretion

Clearance is a fundamental pharmacokinetic parameter that quantifies the efficiency with which a drug is eliminated from the systemic circulation, reflecting the relationship between drug concentration and its rate of removal from the body. A lower clearance rate is typically associated with extended systemic exposure and prolonged residence time. In this study, the predicted clearance values for the designed compounds were found to be higher than that of Enasidenib, as presented in **Table S6**. Specifically, the derivatives P1b/P2b (exo/endo), P1c/P2c (exo/endo), and P1d/P2d (exo/endo) exhibit relatively lower elimination efficiency, suggesting a longer duration of action and potential accumulation in vivo. These findings highlight the importance of balancing metabolic stability with therapeutic efficacy when considering these molecules as drug candidates.

Toxicity

The Ames test, a standard assay used during early phases of drug development, serves to identify potential mutagenic and genotoxic effects that may pose risks such as teratogenicity or carcinogenicity[59]. As summarized in **Table S6**, the designed compounds P1b/P2b (exo/endo), P1c/P2c (exo/endo), and P1d/P2d (exo/endo) exhibited no mutagenic activity, indicating an absence of genotoxic potential. Hepatotoxicity was also evaluated as part of the comprehensive toxicity assessment, and all six novel inhibitors were predicted to be non-hepatotoxic. Moreover, none of the synthesized norcantharimide derivatives, bearing ketone substituents, were found to induce skin sensitization or inhibit the human ether related gene (hERG) potassium channel, which is a critical marker for cardiotoxicity. These findings collectively support the favorable toxicological profile of the proposed molecules.

Furthermore, the predicted LD50 values, presented in **Table S6**, were relatively high, suggesting low acute toxicity and lethality only at substantially high doses. Taken together, the novel norcantharimide derivatives exhibit improved pharmacokinetic and safety properties compared to the reference compound, enasidenib, while meeting Lipinski's rule of five (**Table 4**), as well as the perfect categorical of Veber's rule as shown in **Table S4**. These results position the proposed compounds as promising candidates for further development as novel therapeutic inhibitors in the treatment of hematological malignancies.

3.6. Exploring the interaction of Norcantharimide compounds substituted with a ketonic function with the Main Protease (Mpro) of blood cancer

Following an in-depth evaluation of the intrinsic molecular characteristics and the predicted ADMET profiles (Absorption, Distribution, Metabolism, Excretion, and Toxicity) of the six designed compounds, the next stage of this investigation was dedicated to exploring their molecular interactions with a relevant therapeutic target. Previous reports have highlighted the significant anticancer potential of norcantharimide derivatives, particularly those bearing ether substituents[60,61]. Building on these findings, the current study examined the six newly synthesized norcantharimide analogs each functionalized with a ketone moiety (**Fig. S6**) for their inhibitory activity against the main protease implicated in acute myeloid leukemia (AML). This protease plays a central role in the proteolytic processing of key proteins involved in AML progression, making it a strategic target for the development of novel anticancer agents.

To evaluate the binding potential of the designed compounds, molecular docking techniques were employed, offering a predictive framework to estimate their affinity toward a selected protein target. This approach involves the construction of a three-dimensional (3D) model of the protein's active site, followed by the virtual screening of candidate molecules to identify those capable of occupying the binding pocket and forming favorable non-covalent interactions. By simulating ligand–protein interactions, this method enables the prediction of binding conformations, interaction energies, and the identification of key molecular contacts, thereby offering valuable insights into the potential mechanism of action. In this study, the crystallographic structure of a protease associated with blood cancer (PDB ID: 5NAT) was selected as the molecular target. As reported in **Table S7**, all six norcantharimide-based derivatives (P1b(exo)–P2d(endo)) exhibited strong binding affinities, characterized by low and negative binding energy values. These affinities were consistently more favorable than those of the reference compound, Enasidenib, suggesting superior interaction potential with the target protease[62]. Furthermore, a comparative docking analysis was performed between the designed ligands and Enasidenib (PubChem CID: 89683805) to explore the nature of their interactions with 5NAT. All tested compounds demonstrated robust binding to the active site, supported by both two-dimensional and three-dimensional visualizations.

These representations highlight the formation of key hydrogen bonds, hydrophobic contacts, and surface complementarity, underscoring the potential of these molecules as promising anticancer candidates. **Table S7**, together with **Figs. 5** and **S8**, (The Docked poses of the six designed compounds (P1b-P2d) and Enasidenib with 5NAT (en 2D et 3D)) illustrates the detailed ligand–protein interaction profiles, demonstrating that compound P2d(endo) achieved the most favorable docking score among the six evaluated candidates, with a binding energy of −7.8 kcal/mol. The remaining compounds depicted in **Table S7** showed slightly less favorable but still significant binding energies, ranked as follows: P1d(exo), P1c(exo), P1b(exo), P2c(endo), and P2b(endo), with values ranging from −7.2 kcal/mol to −7.6 kcal/mol. Specifically, compound P1b(exo) established interactions with five amino acid residues within the active site of 5NAT, including a conventional hydrogen bond with TYR113, in addition to four hydrophobic contacts involving PHE2039, TRP90, VAL86, and ILE87. In contrast, P2b(endo) engaged four residues, forming two conventional hydrogen bonds with HIS2055 and ARG286, complemented by two hydrophobic interactions with PHE2048 and ARG2086. These interaction patterns highlight the structural compatibility and potential binding stability of the designed compounds with the target protease (**Fig. 3**).

Compound P1c(exo) formed a conventional hydrogen bond with residue SER235, in addition to engaging in three hydrophobic interactions of the alkyl type with TYR2105, TRP2101, and PHE2108. A notable π–σ interaction was also observed between P1c(exo) and PHE2108, further stabilizing the complex. Similarly, P2c(endo) exhibited four hydrophobic contacts, involving alkyl interactions with MET2089, CYS2085, PHE2048, and ARG2086, along with a carbon–hydrogen bond interaction with GLU2052. Regarding compound P1d(exo), the molecule established a conventional hydrogen bond

with TYR57 and participated in four hydrophobic interactions with TRP90, PHE130, TYR57, and PHE2039, indicating strong binding within the active site. Finally, compound P2d(endo) was stabilized by two conventional hydrogen bonds formed with residues GLY193 and LYS2192, highlighting its favorable binding characteristics.

Among the evaluated compounds, this molecule exhibited the most favorable binding energy and interaction profile, identifying it as the most promising candidate for subsequent molecular dynamics (MD) simulations to assess the stability of the ligand–protein complex. Previous studies have highlighted the essential amino acid residues involved in the binding of enasidenib within the active site of its target protein, including PRO90, LEU59, ALA61A, ALA61B, VAL89, ALA88, LEU86, ARG87, VAL85, GLY62, LYS63, GLN65, VAL64, ASP84, and LEU104[63]. Consistent with these findings, our docking analysis revealed that enasidenib establishes multiple interactions within the binding pocket, notably ten hydrophobic contacts. These include two π–π stacking interactions with TYR2105 and PHE2039, and five alkyl-type hydrophobic interactions involving PHE77, VAL86, ILE87, PHE130, and TYR2105. Additionally, the binding is further stabilized by a π–cation interaction with LYS121, a π–sigma interaction with TRP90, and a halogen interaction with TRP2103. Collectively, these interactions underscore the strong affinity of enasidenib for the selected protein target and validate its efficacy as a reference inhibitor.

3.8 Molecular dynamics simulations

The analysis of root-mean-square deviation (RMSD) provides valuable insight into the conformational stability and integrity of the protein–ligand complex throughout the molecular dynamics (MD) simulation. As illustrated in **Fig. 6**, the RMSD profiles of the ligand (in pink), the protein's Cα atoms (in blue), and the fitted complex (lig fit prot, in magenta) were monitored over the entire simulation period. The ligand exhibited exceptional stability, maintaining an RMSD around 0.25 Å with minimal fluctuations (~0.01 Å), indicating a highly consistent binding conformation.

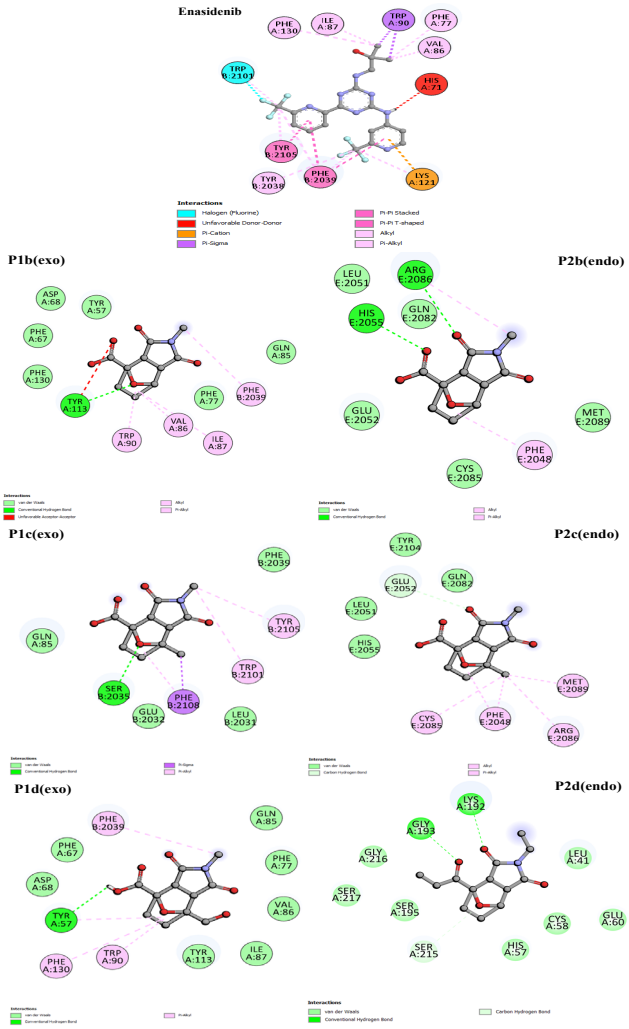

Fig. 5. Docked poses of the six designed compounds (P1b-P2d) and Enasidenib with 5NAT.

The protein backbone RMSD ranged between 2.0 Å and 2.8 Å, stabilizing around an average value of 2.65 Å during the final 50 ns of the trajectory. Notably, the absence of abrupt shifts or flips suggests that no significant conformational changes occurred during the simulation. The protein–ligand complex showed RMSD values within the range of 2.5–3.0 Å, further supporting the structural stability of the system, particularly over the final 40 ns. Root-mean-square fluctuation (RMSF) analysis, depicted in **Fig. 7**, revealed that most residues exhibited fluctuations below 2 Å. However, increased mobility was observed in specific regions, notably between residues 70–80 and 100–110, where fluctuations exceeded 3 Å. Importantly, residues involved in direct interactions with the ligand showed RMSF values below 1 Å, suggesting a stabilizing effect of the ligand on the local protein environment.

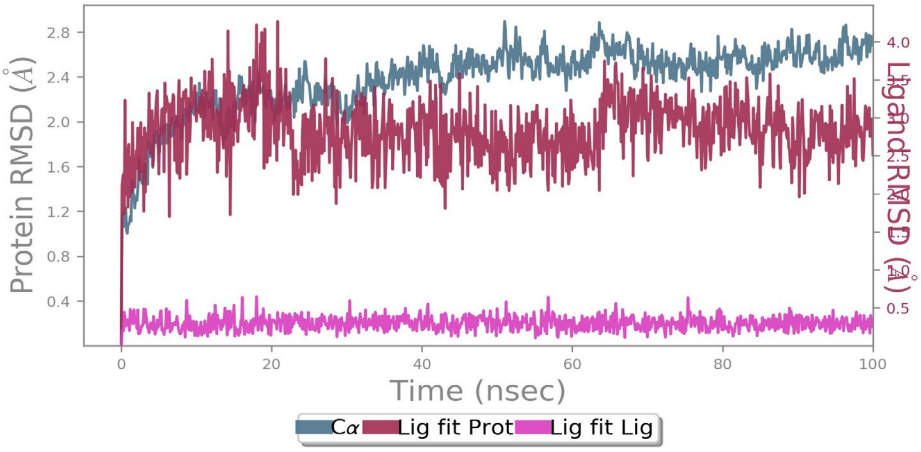

Fig 6. the variation of the RMSD of the ligand P2d, the protein, and the complex throughout a dynamic simulation of 100 ns.

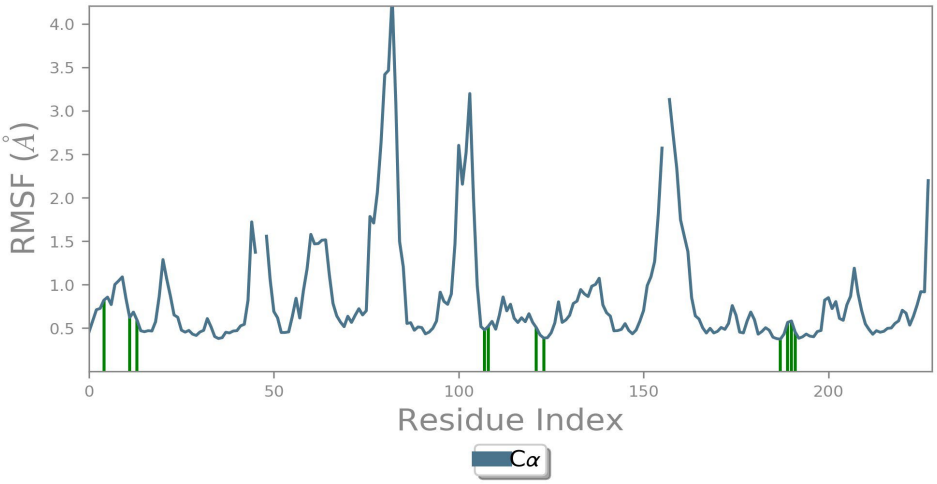

Fig. 7. RMSF variation of the protein' Cα. The protein-P2d interactions are presented in green.

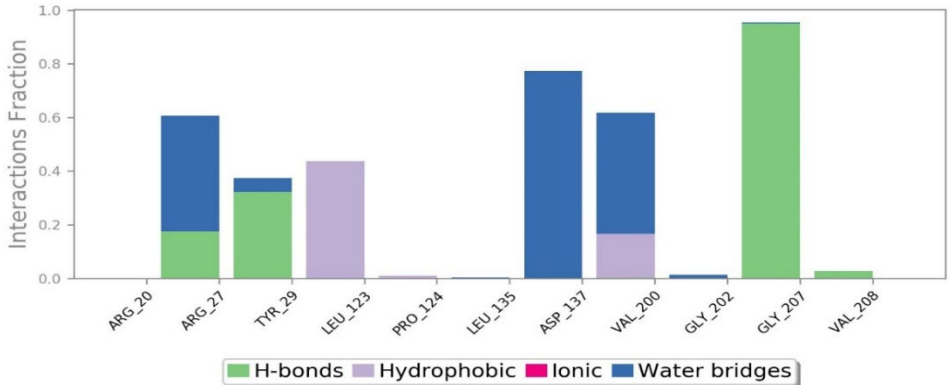

Fig. 8. Protein-P2d interaction diagram and the interaction fractions.

Fig. 8 presents a detailed profile of protein–ligand contacts throughout the simulation. Hydrogen bonds and water-mediated bridges were the predominant interaction types, especially involving residues GLY207, TYR29, ARG27, ASP137, and VAL200. Hydrophobic contacts were also observed, notably with LEU123 and VAL200. Among all interacting residues, GLY207, VAL200, ASP137, LEU123, TYR29, and ARG27 exhibited the highest contact persistence, indicating their crucial role in maintaining the structural integrity and binding stability of the complex.

In **Fig. 9**, the physicochemical and surface properties of the ligand were thoroughly examined through the evaluation of several key descriptors, including the radius of gyration (rGyr), solvent-accessible surface area (SASA), molecular surface area (MolSA), and polar surface area (PSA). The rGyr, which reflects the spatial distribution and overall compactness of the ligand by calculating the mean atomic distance from the molecule's center of mass, remained stable at approximately 2.6 Å throughout the simulation. This consistent value indicates that the ligand retained a compact and stable conformation. MolSA values, representing the total surface area defined by the van der Waals surface, fluctuated within a narrow range of 198–201 Å², suggesting structural uniformity. The PSA, a critical parameter associated with hydrogen bonding capacity and aqueous solubility, displayed a mean value of 153 Å², highlighting the polar character of the ligand. The SASA, which accounts for the solvent-exposed surface area of the molecule, averaged 130 Å², providing further insight into the extent of the ligand's interaction with the surrounding solvent environment. Collectively, these parameters underline the structural stability and surface behavior of the ligand in the simulated biological context.

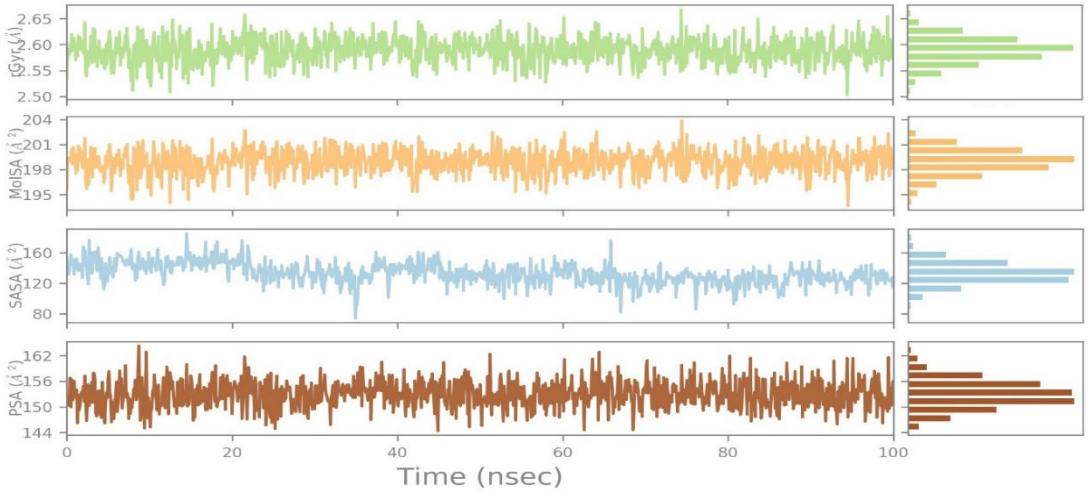

Fig. 9. P2d ligand properties variation during 100 ns of simulation.

4. Conclusion

This study presents a dual theoretical investigation combining cycloaddition reactivity and anticancer drug design. The (4+2) cycloaddition between 1-(furan-2-yl)propan-1-one and 1-R-1H-pyrrole-2,5-dione was explored using DFT at the M06/6-311++G(d,p) level. Analysis of kinetic and thermodynamic parameters in both gas and aqueous phases confirmed a regioselective and asynchronous mechanism. MEDT interpretation, complemented by ELF and Wiberg index analysis, revealed a one-step, two-stage bond formation. NCI analysis further highlighted the role of weak interactions in guiding the transition states. In parallel, a novel approach targeting blood cancer was proposed through the inhibition of the Mpro protease using ketone-functionalized norcantharimide derivatives. Docking studies identified P2d(endo) and P1d(exo) as promising candidates with strong binding affinities and key interactions within the active site. ADMET profiling indicated favorable pharmacokinetics and low toxicity across all designed compounds. Molecular dynamics simulations over 100 ns confirmed the stability of P2d, supported by consistent structural parameters such as radius of gyration, solvent-accessible surface area, and polar surface area. Altogether, this study offers mechanistic insight into Diels–Alder reactivity and proposes a new direction in the design of bioactive compounds against blood cancer, paving the way for future experimental validation.

References

1. Chaudhary M., Kaur G., Kaur N., Kaur P. (**2025**) A Brief Review on Recent Developments in Diels-alder Reactions. *COS* 22, 2–23.
2. Yeingst T. J., Helton A. M., Hayes D. J. (**2024**) Applications of Diels–Alder Chemistry in Biomaterials and Drug Delivery. *Macromolecular Bioscience* 24, 2400274.

3. Zhou Y., Gao G., Li X., Chen W. (**2025**) Diels-Alder reaction in hydrogel synthesis: Mechanisms and functional aspects. *J Biomater Appl* 39, 828–839.
4. Domingo L. R., Aurell M. J., Pérez P., Contreras R. (**2002**) Quantitative characterization of the global electrophilicity power of common diene/dienophile pairs in Diels–Alder reactions. *Tetrahedron* 58, 4417–4423.
5. Ríos-Gutiérrez M., Domingo L. R. (**2019**) Unravelling the Mysteries of the [3+2] Cycloaddition Reactions. *Eur J Org Chem* 2019, 267–282.
6. Jasiński R., Kula K., Łapczuk-Krygier A., Dresler E. (**2014**) An experimental and theoretical study of the hetero Diels–Alder reactions between (E)-2-aryl-1-cyano-1-nitroethenes and ethyl vinyl ether: one-step or zwitterionic, two-step mechanism? *Reac Kinet Mech Cat* 113, 333–345.
7. Jasiński R., Mirosław B., Demchuk O. M., Babyuk D., Łapczuk-Krygier A. (**2016**) In the search for experimental and quantumchemical evidence for zwitterionic nature of (2E)-3-[4-(dimethylamino) phenyl]-2-nitroprop-2-enenitrile–An extreme example of donor–π–acceptor push–pull molecule. *Journal of Molecular Structure* 1108, 689–697.
8. Domingo L. R., Picher M. T., Arroyo P. (**2006**) Towards an Understanding of the Polar Diels–Alder Reactions of Nitrosoalkenes with Enamines: A Theoretical Study. *Eur J Org Chem* 2006, 2570–2580.
9. Sahrane M., Marakchi K., Ghailane R. (**2021**) Theoretical study of the Diels–Alder reaction of 3-bromo-1-phenylprop-2-ynone with furan and 2-methylfuran. *Theor Chem Acc* 140, 108.
10. Boutadghart T., Ghailane R. (**2023**) A molecular electron density theory study of asymmetric Diels–Alder [4 + 2] reaction's mechanism of furan with three substituted alkynes (5-R substituted-3-(3-(phenylsulfonyl)-propioloyl)-oxazolidin-2-one). *J Mol Model* 29, 290.
11. Boutadghart T., Ghailane R. (**2023**) DFT mechanistic study of [4+ 2] cycloaddition reactions of 1-methyl-1H-pyrrole-2, 5-dione with furoic acid, anticancer Activity, molecular modeling and ADMET properties of new products from the Norcantharimide family substituted by a carboxylic acid. *Computational and Theoretical Chemistry* 1230, 114384.
12. Cioc R. C., Smak T. J., Crockatt M., Van Der Waal J. C., Bruijnincx P. C. (**2021**) Furoic acid and derivatives as atypical dienes in Diels–Alder reactions. *Green Chemistry* 23, 5503–5510.
13. Hill T. A., Stewart S. G., Gordon C. P., Ackland S. P., Gilbert J., Sauer B., Sakoff J. A., McCluskey A. (**2007**) Norcantharimides, synthesis and anticancer activity: Synthesis of new norcantharidin analogues and their anticancer evaluation. *Bioorganic & medicinal chemistry* 15, 6126–6134.
14. Satyanarayana V. S. V., Rakshit M., Sivakumar A. (**2011**) Microwave-assisted synthesis of 2, 4, 5-triphenyl-1H-imidazole containing Schiff base derivatives with potential antioxidant and anticancer activities. *Asian J. Chem* 23, 1212–1218.
15. Kula K., Jasiński R. (**2025**) On the Question of the Application Potential and the Molecular Mechanism of the Formation of 1, 3-Diaryl-5-Nitropyrazoles from Trichloromethylated Diarylnitropyrazolines. *Molecules* 30, 4306.
16. Janowski M., Kula K., Krawczyk P., Jasiński R. (**2025**) New 4-(Morpholin-4-Yl)-3-Nitrobenzhydrazide Based Scaffold: Synthesis, Structural Insights, and Biological Evaluation. *Molecules* 30, 3343.
17. Bryantsev V. S., Diallo M. S., Van Duin A. C. T., Goddard W. A. (**2009**) Evaluation of B3LYP, X3LYP, and M06-Class Density Functionals for Predicting the Binding Energies of Neutral, Protonated, and Deprotonated Water Clusters. *J. Chem. Theory Comput.* 5, 1016–1026.
18. Zhao Y., Truhlar D. G. (**2008**) Density Functionals with Broad Applicability in Chemistry. *Acc. Chem. Res.* 41, 157–167.
19. Ghahremanpour M. M., Van Maaren P. J., Van Der Spoel D. (**2018**) The Alexandria library, a quantum-chemical database of molecular properties for force field development. *Scientific data* 5, 1–10.
20. Schlegel H. B. (**1982**) Optimization of equilibrium geometries and transition structures. *J Comput Chem* 3, 214–218.
21. Fukui K. (**1970**) Formulation of the reaction coordinate. *J. Phys. Chem.* 74, 4161–4163.
22. Gonzalez C., Schlegel H. B. (**1990**) Reaction path following in mass-weighted internal coordinates. *J. Phys. Chem.* 94, 5523–5527.
23. Tomasi J., Persico M. (**1994**) Molecular Interactions in Solution: An Overview of Methods Based on Continuous Distributions of the Solvent. *Chem. Rev.* 94, 2027–2094.
24. Cossi M., Barone V., Cammi R., Tomasi J. (**1996**) Ab initio study of solvated molecules: a new implementation of the polarizable continuum model. *Chemical Physics Letters* 255, 327–335.
25. Mennucci B., Cancès E., Tomasi J. (**1997**) Evaluation of Solvent Effects in Isotropic and Anisotropic Dielectrics and in Ionic Solutions with a Unified Integral Equation Method: Theoretical Bases, Computational Implementation, and Numerical Applications. *J. Phys. Chem. B* 101, 10506–10517.
26. Domingo L. R., Ríos-Gutiérrez M. A. (**2023**) useful classification of organic reactions based on the flux of the electron density. *Scientiae Radices* 2, 1–24.
27. Aitouna A. O., Rossafi B., El Alaoui H. E. A., Zeroual A. (**2025**) Molecular Electron Density Study on the [3+ 2] Cycloaddition Reaction between Diphenylnitrylimine and Cinnamaldehyde. *Sci. Rad* 4, 18–28.
28. Domingo L. R., Ríos-Gutiérrez M., Pérez P. (**2025**) Electrophilicity ømega and Nucleophilicity N Scales for Cationic and Anionic Species. *Sci. Rad* 4, 1–17.

29. Silvi B., Savin A. (**1994**) Classification of chemical bonds based on topological analysis of electron localization functions. *Nature* 371, 683–686.
30. Lu T., Chen F. (**2012**) Multiwfn: A multifunctional wavefunction analyzer. *J Comput Chem* 33, 580–592.
31. Bader R. F., Essén H. (**1984**) The characterization of atomic interactions. *The Journal of chemical physics* 80, 1943–1960.
32. Humphrey W., Dalke A., Schulten K. (**1996**) VMD: visual molecular dynamics. *Journal of molecular graphics* 14, 33–38.
33. Lefebvre C., Rubez G., Khartabil H., Boisson J. C., Contreras-García J., Hénon E. (**2017**) Accurately extracting the signature of intermolecular interactions present in the NCI plot of the reduced density gradient versus electron density. *Physical Chemistry Chemical Physics* 19, 17928–17936.
34. Tan S. L., Jotani M. M., Tiekink E. R. (**2019**) Utilizing Hirshfeld surface calculations, non-covalent interaction (NCI) plots and the calculation of interaction energies in the analysis of molecular packing. *Structure Reports* 75, 308–318.
35. Daina A., Michielin O., Zoete V. (**2017**) SwissADME: a free web tool to evaluate pharmacokinetics, drug-likeness and medicinal chemistry friendliness of small molecules. *Scientific reports* 7, 42717.
36. Pires D. E. V., Blundell T. L., Ascher D. B. (**2015**) pkCSM: Predicting Small-Molecule Pharmacokinetic and Toxicity Properties Using Graph-Based Signatures. *J. Med. Chem.* 58, 4066–4072.
37. Lorthiois E., Goller M., Montalbetti C., Kretz O., Guba W., Glickman F., Kessler P., Weiss A., Popp A., Micallef S., Gassner A., Fischer H., Gikic D., Feifel R., Schuler F., Bezençon O., Bitterer T., Ottaviani M., Wright M., Zécri F., (**2017**) Discovery of Highly Potent and Selective Small-Molecule Reversible Factor D Inhibitors Demonstrating Alternative Complement Pathway Inhibition in Vivo. *J. Med. Chem.* 60, 5717–5735.
38. Liu K., Kokubo H. (**2020**) Prediction of ligand binding mode among multiple cross-docking poses by molecular dynamics simulations. *J Comput Aided Mol Des* 34, 1195–1205.
39. Hsieh C. H., Chao K. S. C., Liao H. F., Chen Y. J. (**2013**) Norcantharidin, derivative of cantharidin, for cancer stem cells. https://www.cabidigitallibrary.org/doi/full/10.5555/20143060365.
40. Kouranov A., Xie L., de la Cruz J., Chen L., Westbrook J., Bourne P. E., Berman H. M. (**2006**) The RCSB PDB information portal for structural genomics. *Nucleic acids research* 34, D302–D305.
41. Morris G. M., Huey R., Lindstrom W., Sanner M. F., Belew R. K., Goodsell D. S., Olson A. J. (**2009**) AutoDock4 and AutoDockTools4: Automated docking with selective receptor flexibility. *J Comput Chem* 30, 2785–2791.
42. Huey R., Morris G. M., Forli S. (**2012**) Using AutoDock 4 and AutoDock vina with AutoDockTools: a tutorial. *The Scripps Research Institute Molecular Graphics Laboratory* 10550, 1000.
43. Sharma S., Sharma A., Gupta U. (**2021**) Molecular Docking studies on the Anti-fungal activity of Allium sativum (Garlic) against Mucormycosis (black fungus) by BIOVIA discovery studio visualizer 21.1. 0.0. *Annals of Antivirals and Antiretrovirals* 5, 028–032.
44. Klepeis J. L., Lindorff-Larsen K., Dror R. O., Shaw D. E. (**2009**) Long-timescale molecular dynamics simulations of protein structure and function. *Current opinion in structural biology* 19, 120–127.
45. Jaramillo P., Domingo L. R., Chamorro E., Pérez P. (**2008**) A further exploration of a nucleophilicity index based on the gas-phase ionization potentials. *Journal of Molecular Structure: THEOCHEM* 865, 68–72.
46. Domingo L. R., Aurell M. J., Pérez P., Contreras R. (**2002**) Quantitative characterization of the global electrophilicity power of common diene/dienophile pairs in Diels–Alder reactions. *Tetrahedron* 58, 4417–4423.
47. Domingo L. R., Pérez P., Sáez J. A. (**2013**) Understanding the local reactivity in polar organic reactions through electrophilic and nucleophilic Parr functions. *RSC advances* 3, 1486–1494.
48. Domingo L. R. (**2014**) A new C–C bond formation model based on the quantum chemical topology of electron density. *RSC Advances* 4, 32415–32428.
49. Andrés J., González-Navarrete P., Safont V. S. (**2014**) Unraveling reaction mechanisms by means of Quantum Chemical Topology Analysis. *Int J of Quantum Chemistry* 114, 1239–1252.
50. Bhandari S., Dunietz B. D. (**2019**) Quantitative Accuracy in Calculating Charge Transfer State Energies in Solvated Molecular Complexes Using a Screened Range Separated Hybrid Functional within a Polarized Continuum Model. *J. Chem. Theory Comput.* 15, 4305–4311.
51. Putz M. V. (**2020**) *New Frontiers in Nanochemistry: Concepts, Theories, and Trends: Volume 2: Topological Nanochemistry*. CRC Press.
52. Contreras-García J., Yan W., Johnson E. R. (**2011**) Analysis of Hydrogen-Bond Interaction Potentials from the Electron Density: Integration of Noncovalent Interaction Regions. *J. Phys. Chem. A* 115, 12983–12990.
53. Contreras-García J., Johnson E. R., Keinan S., Chaudret R., Piquemal J. P., Beratan D. N., Yang W. (**2011**) NCIPLOT: A Program for Plotting Noncovalent Interaction Regions. *J. Chem. Theory Comput.* 7, 625–632.
54. Lefebvre C., Rubez G., Khartabil H., Boisson J. C., Contreras-García J., Hénon E. (**2017**) Accurately extracting the signature of intermolecular interactions present in the NCI plot of the reduced density gradient versus electron density. *Physical Chemistry Chemical Physics* 19, 17928–17936.
55. Vaught A. (**1996**) Graphing with Gnuplot and Xmgr: two graphing packages available under linux. *Linux Journal* 1996, 7-es.
56. Vistoli G., Pedretti A., Testa B. (**2008**) Assessing drug-likeness–what are we missing? *Drug discovery today* 13, 285–294.

57. Poongavanam V., Danelius E., Peintner S., Alcaraz L., Caron G., Cummings M. D., Wlodek S., Erdélyi M., Hawkins P. C., Ermondi G., Doak B. C., Kihlberg J. (**2021**) Predicting the permeability of macrocycles from conformational sampling–limitations of molecular flexibility. *Journal of Pharmaceutical Sciences* 110, 301–313.
58. Ertl P., Schuffenhauer A. (**2009**) Estimation of synthetic accessibility score of drug-like molecules based on molecular complexity and fragment contributions. *J Cheminform* 1, 8.
59. Clive D. (**1985**) Mutagenicity in drug development: interpretation and significance of test results. *Regulatory Toxicology and Pharmacology* 5, 79–100.
60. Hill T. A., Stewart S. G., Ackland S. P., Gilbert J., Sauer B., Sakoff J. A., McCluskey A. (**2007**) Heterocyclic substituted cantharidin and norcantharidin analogues—synthesis, protein phosphatase (1 and 2A) inhibition, and anti-cancer activity. *Bioorganic & medicinal chemistry letters* 17, 3392–3397.
61. Wang G., Dong J., Deng L. (**2018**) Overview of cantharidin and its analogues. *Current medicinal chemistry* 25, 2034–2044.
62. Koubi Y., El Khatabi K., Aanouz I., El-Mernissi R., Ajana M. A., Bouachrine M., Lakhlifi T. (**2024**) Use of 1, 2, 3-triazole Derivatives as Potential Inhibitors Blood Cancer, 3D-QSAR, Molecular Docking, and In-silico Pharmacokinetic and Toxicological Studies. http://nanobioletters.com/wp-content/uploads/2024/07/LIANBS131.048.pdf.
63. Alom M. M., Faruqe M. O., Molla M. K. I., Rahman M. M. (**2023**) Exploring Prognostic Biomarkers of Acute Myeloid Leukemia to Determine Its Most Effective Drugs from the FDA-Approved List through Molecular Docking and Dynamic Simulation. *BioMed Research International* 2023, 1946703.

© 2026 by the authors; licensee Growing Science, Canada. This is an open access article distributed under the terms and conditions of the Creative Commons Attribution (CC-BY) license (http://creativecommons.org/licenses/by/4.0/).